



Electrochemical XPS investigation of metal exsolution on SOFC electrodes: Controlling the electrode oxygen partial pressure in ultra-high-vacuum



Andreas Nenning*, Jürgen Fleig

TU Vienna, Institute for Chemical Technologies and Analytics, Getreidemarkt 9, Vienna 1060, Austria

ARTICLE INFO

Keywords:

Solid oxide fuel cell
Mixed conductor
Exsolution
Thin film
Over potential
XPS

ABSTRACT

Mixed conducting oxides gain increasing interest as anode materials in solid oxide fuel cells (SOFCs), due to their large electrochemically active surface area and excellent redox stability, compared to state-of-the-art Ni-Yttria-Stabilized Zirconia cermets. However, further optimization of these materials requires more information on the surface chemistry and the reaction mechanisms. Here we present a new concept for electrochemical XPS measurements close to SOFC anode operation conditions even in a UHV chamber. Application of a voltage versus an oxygen buffering reference electrode enables control of the effective oxygen partial pressure in the investigated mixed conducting thin film working electrode within the range that is typical for SOFC anodes or SOEC cathodes. A lower limit is given by the reductive decomposition of the working electrode. The virtual absence of molecules in the gas phase of the UHV chamber largely prohibits presence of atmospheric adsorbates. However, surface oxidation states of metal ions can be tuned by the over potential, and exsolution of metallic species can be monitored in situ. With this technique, we investigated the oxygen partial pressure dependent oxidation states of transition metals in $\text{La}_{0.6}\text{Sr}_{0.4}\text{FeO}_{3-\delta}$, $\text{SrTi}_{0.3}\text{Fe}_{0.7}\text{O}_{3-\delta}$ and $\text{La}_{0.7}\text{Sr}_{0.2}\text{Cr}_{0.9}\text{Ni}_{0.1}\text{O}_{3-\delta}$ thin film electrodes. When the oxygen partial pressure in the working electrode goes sufficiently below the NiO/Ni and FeO/Fe redox pairs, the exsolution of metallic Ni or Fe nanoparticles could be monitored in-situ. While most oxides are easier to reduce at the surface, Cr on the $\text{La}_{0.7}\text{Sr}_{0.2}\text{Cr}_{0.9}\text{Ni}_{0.1}\text{O}_{3-\delta}$ surface turns out to be more oxidized than the bulk and can include a Cr^{6+} species.

Introduction

In solid oxide fuel/electrolysis cell (SOFC/SOEC) research, UHV-based photoelectron spectroscopy is typically used ex-situ to detect compositional changes of materials after various types of surface treatment or after cell operation [1–3]. However, the very different temperature, polarization state and atmospheric conditions during electrode operation and analysis limit the conclusiveness of such measurements. Frequently, only information on the surface composition is unambiguously accessible, while further chemical information (e.g. on oxidation states and adsorbates) likely differs strongly relative to operating conditions. These problems can be mostly overcome in ambient pressure XPS (APXPS) measurements. These can even be conducted during electrochemical polarization when a proper electrochemical model cell is used [4,5]. This has been done extensively on ceria-based materials in reducing atmospheres [6–11], and on perovskite-type mixed conductors [12–16].

However, APXPS is an expensive technique, which is for most researchers only available at synchrotron beamlines. Moreover, the

identification of reacting or catalysing surface species can be rather challenging, since only a part of the surface species observed in APXPS are actually caused by atmospheric adsorbates. In the XPS spectra, surface components and their changes upon polarization can also originate from point defects at or near the surface. These defects are likely to differ from the bulk, e.g. from a lowered enthalpy for oxygen vacancy formation or transition-metal reduction. Further effects may also be caused by a surface space charge zone. Higher reducibility at the surface was already shown for ceria [7], $\text{La}_{0.6}\text{Sr}_{0.4}\text{FeO}_{3-\delta}$ (LSF) and $\text{SrTi}_{0.7}\text{Fe}_{0.3}\text{O}_{3-\delta}$ (STF) [12]. A further common phenomenon is a varying cation composition at the surface, e.g. segregation of certain cations such as Sr [1,2,17,18]. Given the amount of possible origins for surface species that are detectable in APXPS, it is very challenging to identify those that are relevant in electrochemical surface reactions.

In this paper we present a new experiment design, in which electrochemical XPS measurements are performed on a mixed conducting thin film electrode on a solid oxide model cell in ultrahigh vacuum. The setup allows control of the effective oxygen partial pressure in the thin film electrode, simply by adjusting the voltage, even when a gas phase

* Corresponding author.

E-mail address: andreas.nenning@tuwien.ac.at (A. Nenning).

<https://doi.org/10.1016/j.susc.2018.10.006>

Received 23 May 2018; Received in revised form 3 September 2018; Accepted 3 October 2018

Available online 11 October 2018

0039-6028/ © 2018 Published by Elsevier B.V.

is absent. Thereby we can observe oxygen partial pressure dependent transition metal oxidation states and Fermi level changes. The XPS spectra collected with this technique are expected to contain the electrode surface related features that are expected also in operation, but without atmospheric adsorbates. Therefore, this method can serve as a valuable reference for APXPS measurements to help defining the spectral features that are actually caused by adsorbates. Also the exsolution of metallic particles out of the bulk can be monitored in situ. Still, to the authors' best knowledge, such UHV XPS studies on polarized solid oxide cells were not performed so far.

First we present the electrochemical cell design and testing conditions that are suited for electrochemical XPS (EC-XPS) characterization of SOFC anode materials in UHV conditions. The model cell contains a thick electrolyte (0.5 mm YSZ single crystal), a mixed conducting thin film working electrode and an oxygen nonstoichiometric thick film as combined counter and reference electrode that serves as an oxygen buffer with virtually constant oxygen chemical potential. The working electrode materials $\text{La}_{0.6}\text{Sr}_{0.4}\text{FeO}_{3-\delta}$ (LSF), $\text{SrTi}_{0.3}\text{Fe}_{0.7}\text{O}_{3-\delta}$ (STF) and $\text{La}_{0.7}\text{Sr}_{0.2}\text{Cr}_{0.9}\text{Ni}_{0.1}\text{O}_{3-\delta}$ (LSCr-Ni) are acceptor doped by either partially replacing La^{3+} by Sr^{2+} , or replacing Ti^{4+} by Fe^{3+} . The missing positive charge of the dopant ions is balanced by formation of oxygen vacancies (causing ionic conductivity) and mixed transition metal oxidation states (causing electronic conductivity). Exemplarily, the oxidation states of Fe in LSF and STF and of Ni and Cr in LSCr-Ni are investigated at 600 °C. The results are presented as a function of information depth (by variation of the photoelectron emission angle) and effective working electrode $p\text{O}_2$, which is varied by the cell voltage.

Electrochemical behaviour of a solid oxide cell in ultra-high vacuum

Usually, solid oxide cells with a thin film working electrode are tested in a specific oxidizing or reducing gas environment. Due to the difficulties of a proper reference electrode placement on a solid electrolyte [19], the counter electrode is typically also used as the reference electrode, and designed to have comparatively fast kinetics. Also our cells use a combined counter and reference electrode, with an oxygen partial pressure that is independent of the cell polarisation, so we will name it reference electrode in this work. For cells in ambient atmosphere, a good combined counter and reference electrode can be achieved by using a porous [8,12,20] electrode or one that is much larger than the working electrode [21,22]. This ensures that over potential losses occur primarily in the electrolyte and at the working electrode, and therefore the over potential of the working electrode equals applied voltage minus electrolyte losses [8,12]. In UHV, however, electrochemical oxygen exchange at the surface is negligibly slow, due to the low background pressure. Hence, application of a voltage in UHV does not lead to a steady state ionic current. Unfortunately, an electrode equilibrated in oxidising conditions has a rather high oxygen chemical potential or effective oxygen partial pressure in the electrode bulk ($p\text{O}_2^{\text{WE}}$). At elevated temperature, such an electrode will release significant amounts of O_2 , leading to ill-defined electrode oxygen content and high background pressure in the chamber. SOFC anodes and SOEC cathodes, however, operate at effective oxygen partial pressures below 10^{-12} mbar. With such a low internal partial pressure, the rate of O_2 release is negligible. However also the very low gas phase pressure in the XPS chamber can induce oxidation reactions by O_2 or reduction reactions by H_2 molecules. Still, this very small reaction rate has very little effect on the oxygen chemical potential in the cell because of its very large oxygen buffering capacity in the non-stoichiometric electrodes.

Also without surface oxygen exchange reactions, the applied cell voltage will move oxygen ions through the electrolyte and cause stoichiometric polarisation of the electrodes. With a constant applied voltage there is no DC current, and therefore no over potential losses attributed to electron or ion conduction within the cell. The effective

oxygen partial pressures inside the investigated (working) electrode and counter electrodes are then exactly related by Nernst's equation

$$\frac{p\text{O}_2^{\text{WE}}}{p\text{O}_2^{\text{RE}}} = e^{4\frac{FU}{RT}}, \quad (1)$$

where $p\text{O}_2^{\text{WE}}$ and $p\text{O}_2^{\text{RE}}$ are oxygen partial pressures inside the working and the reference electrodes, respectively, and U is the voltage applied between working and reference electrodes; R , T , F are gas constant, temperature and Faraday's constant, respectively. The $p\text{O}_2$ values inside the material represent the oxygen chemical potential via $\mu_{\text{O}} = \mu_{\text{O}}^0 + RT \ln(p\text{O}_2/1 \text{ bar})$. A solid oxide cell in UHV behaves like an oxygen ion battery that is charged (or discharged) by an externally applied voltage. The idealised equivalent circuit for a solid oxide cell in UHV is therefore a series connection of two capacitors, reflecting the electrode's chemical capacitances. If these capacitances differ strongly in working and reference electrodes, most of the applied voltage drops at the smaller capacitor. In this case, also the effective oxygen partial pressure remains almost constant in the large capacitance (reference) electrode, while changing significantly in the small capacitance (working) electrode. From Eq. (1) we see that if $p\text{O}_2^{\text{RE}}$ is known and constant, it is possible to precisely control $p\text{O}_2^{\text{WE}}$ by the cell voltage. For a stable $p\text{O}_2^{\text{RE}}$, a large oxygen buffer capacity (chemical capacitance) is required, which can be achieved by using an oxygen non-stoichiometric thick film GDC reference electrode and a proper pre-reduction procedure that is elaborated in the experimental section. Accordingly, also in UHV it becomes possible to analyse the surface chemistry of SOFC electrode materials as a function of oxygen partial pressure. It turns out that for the materials used in this study $p\text{O}_2^{\text{WE}}$ can be tuned from the decomposition limit of the electrode up to at least $\sim 10^{-8}$ mbar without significant oxygen loss (higher pressures were not tested).

3. Experimental

3.1. Preparation of targets

Targets for pulsed laser deposition were prepared either by Pecini method ($\text{La}_{0.6}\text{Sr}_{0.4}\text{FeO}_{3-\delta}$ and $\text{La}_{0.7}\text{Sr}_{0.2}\text{Cr}_{0.9}\text{Ni}_{0.1}\text{O}_{3-\delta}$) or solid state reaction ($\text{SrTi}_{0.3}\text{Fe}_{0.7}\text{O}_{3-\delta}$). Powders were calcined at 1000 °C, milled in an agate mortar, isostatically pressed and sintered at 1400 °C in air. The A-site deficient $\text{La}_{0.7}\text{Sr}_{0.2}\text{Cr}_{0.9}\text{Ni}_{0.1}\text{O}_{3-\delta}$ pellet exhibited a small amount of Ni-Cr spinel, shown in Figure S3.

3.2. Preparation of the reference electrode

For the fabrication of a reference (= counter) electrode with high chemical capacitance, $\text{Ce}_{0.8}\text{Gd}_{0.2}\text{O}_{1.9-\delta}$ (GDC, Treibacher AG, Austria), ethyl-cellulose and Terpineole were mixed in a weight ratio of 1:0.2:0.5 and brushed on the rough side of one side polished $10^*10^*0.5 \text{ mm}^3$ yttria stabilised zirconia (YSZ) single crystals. A thin current collecting Pt paste layer was brushed on top of the reference electrode. After drying and sintering for 5 h at 1200 °C in air, the thickness of the porous GDC layer is about 20 μm . While GDC is an ion conductor with small chemical capacitance in oxidizing atmospheres, Ce gets partly reduced to Ce^{3+} in H_2 - H_2O atmosphere, resulting in a sufficiently large chemical capacitance. From literature data [23] we can estimate that our reference electrode has a chemical capacitance of $\sim 300 \text{ mF/cm}^2$ in 1:1 $\text{H}_2 + \text{H}_2\text{O}$ atmosphere at 600 °C. This is in reasonable agreement with the measured capacitance of 150 mF/cm^2 , derived from impedance measurements on samples with porous GDC electrodes on both sides. The capacitance of the counter electrode is thus one to two orders of magnitude larger than the chemical capacitance of our thin film electrodes in the investigated $p\text{O}_2$ ranges [24]. Hence, large changes of $p\text{O}_2^{\text{WE}}$ are possible while $p\text{O}_2^{\text{RE}}$ shifts less by a factor of 10–100. Thus, we assume constant $p\text{O}_2^{\text{RE}}$ in our experimental results.

Table 1
Deposition parameters of the thin film working electrodes.

Material	°C	O ₂ pressure (mbar)	Laser rate	Deposition time	Laser energy	Film thickness
SrTi _{0.3} Fe _{0.7} O ₃	650	0.02	5 Hz	20 min	400 mJ	100 nm
La _{0.6} Sr _{0.4} FeO _{3-δ}	650	0.04	5 Hz	30 min	400 mJ	100 nm
GDC/La _{0.7} Sr _{0.2} Cr _{0.9} Ni _{0.1} O _{3-δ}	650/700°	0.04/0.015	5 Hz + 10 Hz	16 min + 9 min	400 mJ	175 nm + 100 nm

3.3. Deposition of the working electrode and current collector

After fabrication of the reference electrode, a ~70 nm thick mesh-type Ti-Pt current collector (5 μm stripes with 25 μm square holes) was sputter deposited on the polished side of the YSZ substrates and structured by photolithography and argon ion beam etching. On top of the current collector, different SOFC anode materials were deposited by pulsed laser deposition (PLD). The materials and PLD conditions are summarized in Table 1. In case of the La_{0.7}Sr_{0.2}Cr_{0.9}Ni_{0.1}O_{3-δ} (LSCr-Ni) electrode, a Ce_{0.8}Gd_{0.2}O_{2-δ} (GDC) buffer layer was used to avoid reactions between electrode and electrolyte, such as La₂Zr₂O₇ formation. After deposition, the 10*10 mm² samples were fractured into pieces of ~10 mm² area, in order to minimize the relative contribution of the electrical wiring and contacting resistance.

3.4. Pre-reduction procedure

After deposition of the working electrode, the effective oxygen partial pressure in the electrodes corresponds to the mildly oxidizing PLD conditions. Heating of such a cell in UHV would lead to significant oxygen loss and hence bad vacuum in the chamber, combined with drifting oxygen partial pressures in the electrodes. The samples were therefore first reduced at 600 °C in water saturated 2.5% H₂ buffered in Ar, resulting in a H₂:H₂O ratio of about 1:1 and a pO₂ of 1.3*10⁻²⁴ bar. During this pre-reduction step electrochemical impedance spectroscopy was employed to measure the area-specific resistance (ASR) and chemical capacitance of the working electrode, as shown in Fig. 1b. The electrolyte resistance (axes offset in Fig. 1c) is followed by an arc which is largely due to the working electrode; the reference electrodes exhibits a negligible ASR of less than 1 Ωcm², determined from symmetric samples with two porous GDC electrodes. After a reduction time of 30 min, the sample was quenched within a few seconds, which ensured conservation of the equilibrium oxygen nonstoichiometry established at 600 °C in H₂/H₂O.

3.5. Electrochemical XPS measurements in UHV

The electrochemical XPS measurements were carried out using facilities of the “Analytical Instrumentation Center”, Technische Universität

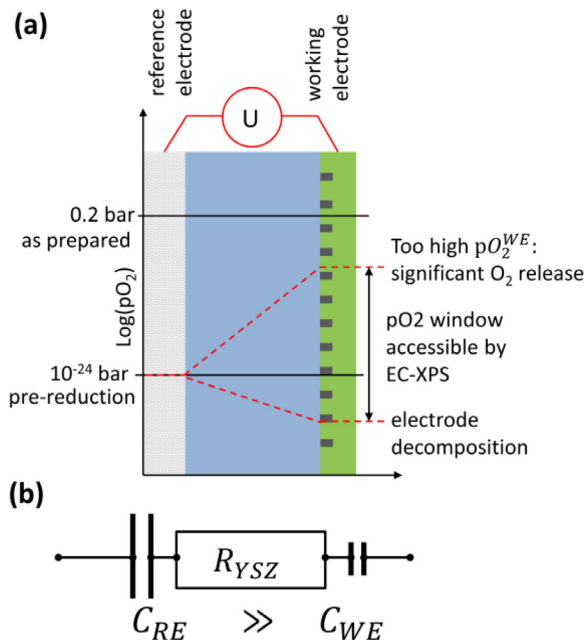


Fig. 2. (a) Sketched distribution of the effective oxygen partial pressure in the model cell after preparation, during pre-reduction and (red dashed lines) during EC-XPS investigation. (b) Equivalent circuit of the cell in UHV.

Wien, Austria. The reduced and quenched electrochemical cell was mounted on a slightly modified 1'-type SPECS sample holder and heated by electron bombardment. Thermally as well as electrical decoupling of model cell and sample holder was achieved by a Pt-covered quartz disk that was mounted on top of a central hole in the sample holder, as shown in Fig. 3. The very low thermal expansion coefficient of quartz minimizes the risk of thermal cracking. The voltage of the electron bombardment filament was limited to 700 V, to avoid artefacts in the XPS spectra caused by elastically and inelastically scattered heating electrons, which appear above 786 eV binding energy with a 1486 eV source. The temperature of the sample was determined from the measured (thermally activated) electrolyte resistance, obtained from the

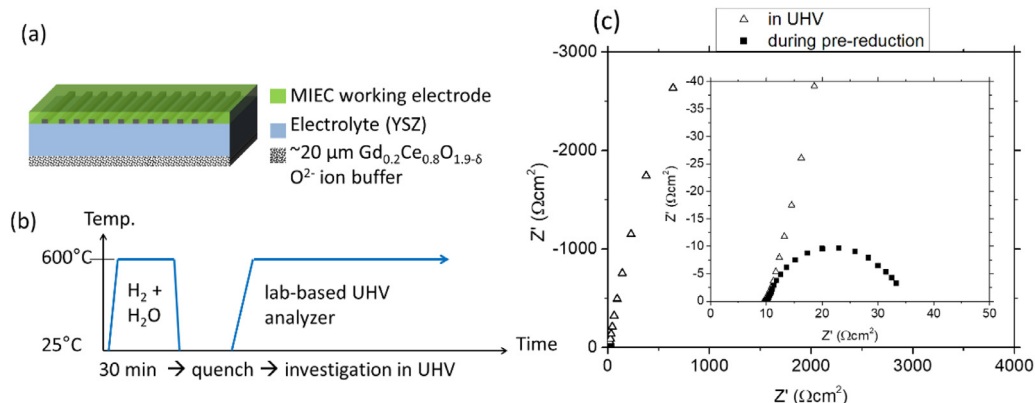


Fig. 1. Sketch of the prepared model cell (a), temperature profile of the pre-reduction procedure (b) and impedance spectra measured on samples with LSF working electrode during pre-reduction and in UHV at 600 °C (c). The inset shows a magnification both spectra.

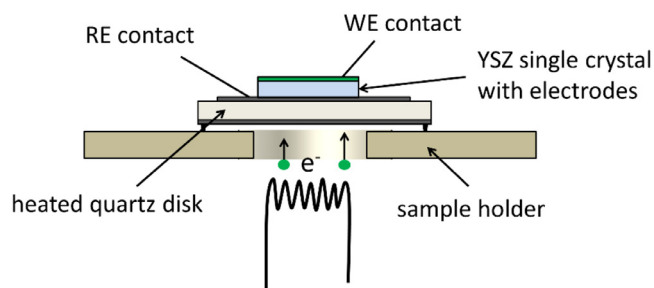


Fig. 3. Cross-section sketch of a model cell mounted on the modified sample holder that is heated by electron bombardment. The quartz disk provides electrical and thermal decoupling from the sample holder.

axes offset of the impedance spectra shown in Fig. 1c. This value was matched to the value measured during pre-reduction ($10 \Omega \text{cm}^2$), which corresponds to 600°C .

The electrical contact and mechanical fixation of the model cell were established by kanthalam tips. These tips penetrate the typically weakly electron conducting MIEC layer and directly contact the embedded Pt current collector beneath the MIEC thin film.

The oxygen non-stoichiometry established in working and reference electrodes during pre-reduction was conserved also during heating in UHV. The effective oxygen partial pressure in the sample (10^{-24} bar vs 1 bar O_2 at 600°C) is too low for release of O_2 from the electrode. Due to the very low pressure in the chamber, the impedance spectrum in UHV (Fig. 1c) displays a very large electrode arc that can be interpreted as negligibly slow oxidation/reduction rate with remaining gas molecules. The capacitance of this arc is still the chemical capacitance of the working electrode and may act as a fingerprint of the oxygen non-stoichiometry [23,25,26]. These chemical capacitances are obtained from an equivalent circuit fit of the electrode arc (parallel connection of resistor and constant phase element) and the values found during pre-reduction and in the XPS chamber are very similar, indicating that the defect chemistry of the pre-reduction is still present at operation temperature in UHV.

XPS spectra were collected using a monochromatic Al K- α source and an angle-resolved SPECS Phoibos WAL analyser at a pass energy of 70 eV. Photoelectrons were collected in between 20 and 80° relative to the surface normal. In order to stay consistent with the treatment of the cell as a solid oxide battery, voltage of the polarised working electrode is indicated relative to a standard oxygen electrode in 1 bar O_2 at 600°C . Since the pre-reduced reference electrode has an oxygen partial pressure of $1.3 \cdot 10^{-24}$ bar, corresponding to a voltage -1.03 V vs O_2 , the effective working electrode potential is -1.03 V vs O_2 when no voltage is applied in UHV

4. Results and discussion

4.1. Evolution of metallic Fe particles from $\text{La}_{0.6}\text{Sr}_{0.4}\text{FeO}_{3-\delta}$ and $\text{SrTi}_{0.3}\text{Fe}_{0.7}\text{O}_{3-\delta}$

Application of a cathodic bias to the working electrode decreases the oxygen partial pressure below 1.03 V vs O_2 . In these conditions the appearance of a Fe^0 phase from LSF and STF was previously found in near ambient pressure XPS measurements during water electrolysis, and linked to increased water splitting kinetics [12,15]. In this paper we provide complementary UHV-based XPS measurements to check whether the presence or absence of a gas phase changes the characteristics of the Fe exsolution. In Fig. 5 we see polarisation dependent Fe2p spectra. The denoted cell potentials were calculated relative to 1 bar O_2 , and the samples were before equilibrated in $\text{H}_2 + \text{H}_2\text{O}$ atmosphere, so the spectrum at -1030 mV corresponds to the pre-equilibration conditions. In the spectra recorded at more reducing conditions (≤ -1030 mV for STF and ≤ -1230 mV for LSF) an additional peak at

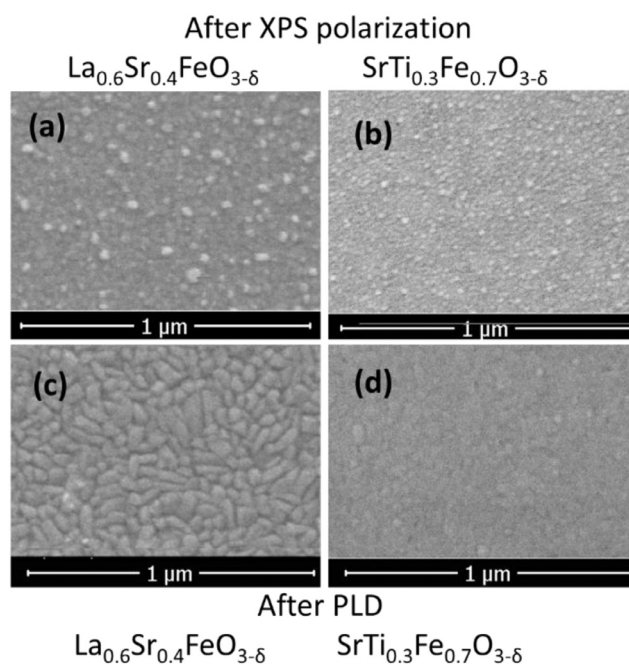


Fig. 4. Comparison of the metal exsolution regimes in LSF and STF. (a,b): After polarization experiments in UHV XPS, under conditions very similar to those used in ambient pressure XPS in Ref. [12], small Fe particles segregate to the surface. (c,d): Surface after PLD, showing no particles.

707 eV appears, which indicates Fe^0 . For STF, some Fe^0 may have already formed during the equilibration step in $\text{H}_2 + \text{H}_2\text{O}$. The in-situ formation of Fe^0 was previously observed by NAP XPS [12,15] measurements at very similar effective oxygen partial pressures. This agreement further confirms the conservation of the oxygen chemical potential after quenching the sample in reducing atmosphere, as sketched in Fig. 1. Also, SEM images in Fig. 4, taken after polarization in UHV support the evolution of metallic nanoparticles. Particle sizes of $5\text{--}20$ nm were observed on STF37, whereas on LSF64, the particles were in the range of $20\text{--}50$ nm. Interestingly, thermogravimetric analysis of LSF64 powder [27] predicts decomposition when the oxygen partial pressure is below 10^{-27} bar at 600°C , corresponding to an over potential of only -1130 mV vs O_2 . However, in the present thin film study, a slightly larger over potential of -1530 mV vs O_2 , corresponding to $\sim 10^{-35}$ bar was needed to show Fe^0 exsolution.

The amount of Fe^0 was determined by a simple fit of the $\text{Fe}2\text{p}_{3/2}$ peak, using only two asymmetric peaks for oxidised and metallic iron, as shown in supplementary figure S1. In the ambient pressure XPS study from Ref. [12], the total Fe2p peak area decreased during the evolution of Fe^0 , and the ratio of metallic and oxidized iron species was independent of the information depth. In contrast, the EC-XPS experiments presented here show a slight increase of total Fe content after the exsolution and more Fe^0 at strongly off-normal electron emission angles, as seen in Fig. 5b. This difference can be understood from the different photoelectron collection techniques in the UHV and NAP analyser. The NAP analyser detects photoelectrons at normal emission angle, and the information depth is varied by changing the photon and photoelectron energy. Since the Fe particles are much larger than the photoelectron mean free path, which is only $0.5\text{--}2$ nm (see SEM images in Fig. 4), the Fe^0 intensity at normal emission is a measure of the surface area fraction covered by metallic Fe. In contrast, the lab-based UHV spectrometer uses an angle-resolved analyser. In this geometry, the projected area of the segregated metallic Fe particles becomes larger at shallow emission angles as sketched in Fig. 5c. This is the reason why an increase in Fe^0 fraction is observed at shallower photoelectron angle, sketched in Fig. 5c.

For substantial applied anodic bias, meaning the spectra labelled

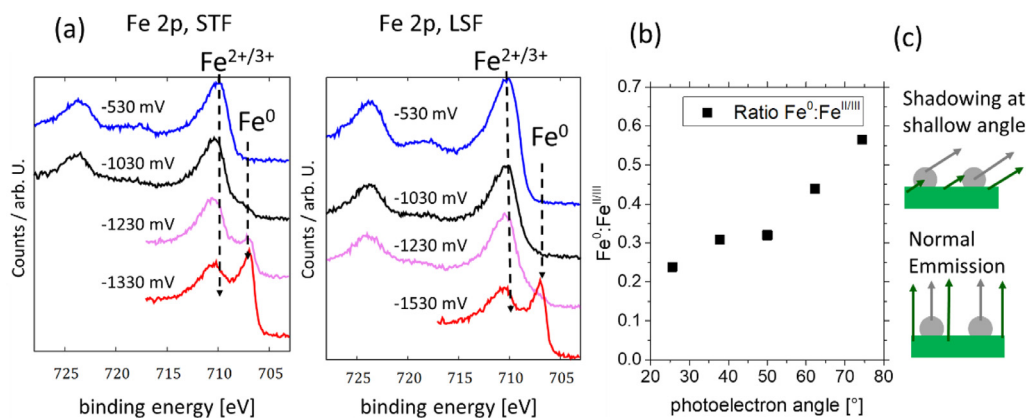


Fig. 5. (a) XPS spectra acquired on pre-reduced LSF and STF electrodes during various levels of electrochemical polarization vs 1 bar O₂ at 600 °C. (b) Ratio of metallic to oxidized Fe component area as a function of the photoelectron angle vs. surface normal, showing increased Fe⁰ fraction at shallow emission. (c) Sketch of morphological shadowing of photoelectrons from the perovskite phase at shallow emission angles.

–530 mV vs O₂, in Fig. 5a, a satellite feature appears at ~719 eV, indicative for Fe³⁺ [27–29]. Thermogravimetric data and defect chemical models predict that most iron should be Fe³⁺, down to the decomposition limit at 1130 mV vs O₂. However, the characteristic Fe³⁺ satellite feature is not visible at –1030 mV vs O₂. In analogy to the conclusions made from APXPS measurements in Ref. [12], more reducing conditions cause a superposition of satellite features from Fe²⁺ (~715 eV) and Fe³⁺ (~719 eV) in similar amounts, which indicates that surface Fe is easier reduced than in the bulk.

Overall, the good agreement of surface Fe oxidation states in the UHV-based and ambient pressure XPS study shows that it is possible to control the oxygen partial pressure and Fe oxidation states in the electrode, even in UHV. We can also conclude that atmospheric adsorbate species have little influence on oxidation states of near surface iron.

4.2. Surface chemistry of La_{0.7}Sr_{0.2}Cr_{0.9}Ni_{0.1}O_{3-δ}

It was shown in literature that chromate-based perovskites doped with Ni can form catalytically active morphologically stable and nanosized Ni exsolutions in reducing conditions at about 800 °C [30–32]. A-site deficiency strongly enhances the exsolution of Ni ions from the B-site of the crystal [31,33]. Furthermore, Ni-doped lanthanum chromite based perovskites were shown exhibit excellent resistance towards carbon formation and reductive decomposition during CO₂ electrolysis [16]. In order to study the Ni exsolution process by electrochemical XPS measurements, we fabricated a model cell with a working electrode consisting of A-site deficient La_{0.7}Sr_{0.2}Cr_{0.9}Ni_{0.1}O_{3-δ} (LSCr-Ni). After initial reduction and quenching XPS spectra were recorded at 600 °C during electrochemical polarisation. For the observation of the Ni oxidation state, the Ni3p peak was used since the Ni2p and La3d_{3/2} peaks overlap. In Fig. 6a polarisation dependent Ni 3p peaks are plotted. The binding energy of ~66.5 eV measured at –1030 and –1480 mV vs O₂ corresponds to Ni⁰ [34], whereas the slightly higher binding energy (67.5 eV) for the spectrum recorded at –530 mV vs O₂ corresponds to the value expected for NiO [34]. These results reveal that Ni exsolutions appear probably already during the pre-reduction procedure, and exsolved particles are oxidised with sufficient anodic bias.

Additional SEM imaging confirmed the Ni exsolution. Particles of 5–10 nm diameter are visible after the XPS polarization experiments at 600 °C (Fig. 6d). For comparison, other samples were also reduced at 800 °C in H₂ + H₂O atmosphere for 5 hours (Fig. 6e). An additional A-site stoichiometric La_{0.8}Sr_{0.2}Cr_{0.9}Ni_{0.1}O_{3-δ} film was deposited with equal conditions as the A-site deficient one and reduced at 800 °C (Fig. 6c). The stoichiometric film did not show any metal exsolutions, whereas the A-site deficient films, which were also used in the EC-XPS measurements, exhibited metallic exsolutions in the 20 nm range. This result is in accordance with a model by Neagu et al. which suggests that A-site deficiency is crucial for the exsolution of B-site dopants [31]. A-

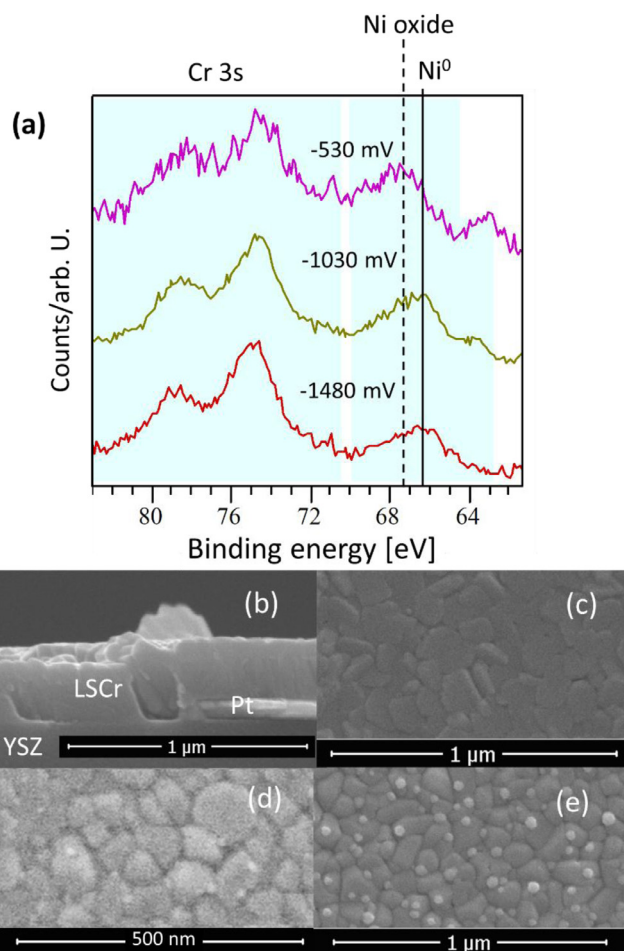


Fig. 6. (a) Ni3p (and Cr3s) XPS spectra, at different cell voltages. (b) SEM cross section of the LSCr-Ni thin film at the border of the current collector. (c) A-site stoichiometric LSCr-Ni film after reduction at 800 °C for 5 h, showing no exsolutions. (d) A-site deficient LSCr-Ni film after the presented polarization experiments in the XPS chamber at 600 °C, showing very small Ni particles and (e) A-site deficient LSCr-Ni film after reduction at 800 °C with larger particles.

site substoichiometric LSCr-Ni can thus be considered as very promising for SOFC anodes or SOEC cathodes. By the exsolution process morphologically stable Ni nanoparticles [33] evolve on the surface of a mixed conducting oxide with high electrochemical stability.

In addition to the exsolution of metallic particles, the (oxygen partial pressure dependent) oxidation states of transition metals that stay in the oxide environment can be explored by EC-XPS. Typically, the different surface energetics make surface ions easier reducible than

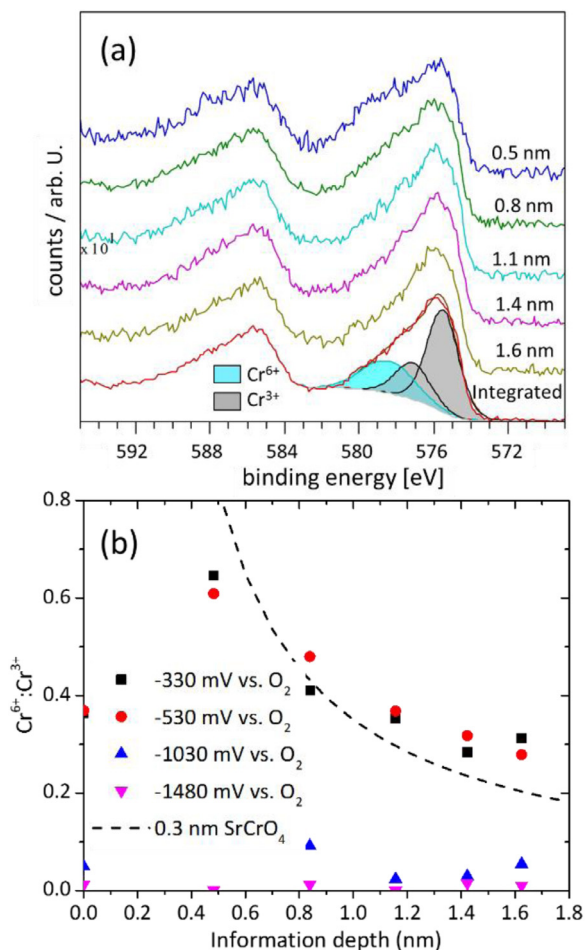


Fig. 7. (a) Angle-resolved Cr2p spectra, with effective information depth and fit indicated, measured at a sample temperature of 600 °C and a p_{O_2} corresponding to -530 mV vs O_2 . (b) $Cr^{6+}:Cr^{3+}$ component ratio plotted as a function of information depth for different polarisation states. The dashed line corresponds to the calculated $Cr^{6+}:Cr^{3+}$ ratio of a uniform 0.3 nm $SrCrO_4$ surface layer on a perovskite with Cr^{3+} only.

the bulk. This was already shown on ceria [7,11] and on LSF64 and STF73 [12]. However, our UHV XPS measurements reveal that for $La_{0.7}Sr_{0.2}Cr_{0.9}Ni_{0.1}O_{3.8}$ this is different. Angle resolved Cr2p spectra are depicted in Fig. 7. These exhibit, apart from the spin-orbit splitting of ~ 9.5 eV, two components at 576 and 579 eV. In accordance with binding energies reported in literature [35,36], these peaks can be attributed to Cr^{3+} and Cr^{6+} , respectively. The Cr^{3+} peak was fitted with two components to account for the asymmetry of this peak, and both components were constrained in relative area, position and FWHM in order to reduce the number of free parameters, and a single peak was used for fitting Cr^{6+} . The Cr^{6+} peak is no more detectable at -1.03 V vs O_2 and lower, shown in supplementary figure S2. Angle resolved photoelectron spectra enable variation of the information depth (d), according to $d = IMFP \cos(\theta)$. IMFP is the photoelectron inelastic mean free path according to the TPP-2M equation [37] (1.8 nm) and θ is the photoelectron angle relative to the surface normal. Emission angle dependent Cr2p spectra recorded at -530 mV vs O_2 are shown in Fig. 7 and reveal a strongly increased Cr^{6+} signal at lower information depth. Accordingly, Cr close to the surface is more oxidized than in the bulk, which is in contrast to the typically more reducible surfaces found e.g. on LSF and STF [12] or Ceria [7,23]. In oxides, Cr^{6+} is mostly known in tetrahedral coordination [35], and it is hence unlikely to be present in a perovskite-type lattice, where B-site cations have octahedral coordination. A more likely explanation of the Cr^{6+}

species is rather related to the phase stability of Sr-doped lanthanum chromite, which was extensively investigated by XRD in Ref. [38] as a function of Sr concentration (10%–30%), oxygen partial pressure and temperature. According to this study, an additional $SrCrO_4$ phase can form, preferentially at low temperature, high oxygen partial pressure and high Sr concentration. When these measurements are extrapolated to our experimental conditions, the pure perovskite single phase is probably still stable. Nevertheless the formation of a $SrCrO_4$ surface layer is possible, especially when considering that Sr is enriched on most perovskite-type surfaces. To test this hypothesis the Cr^{6+}/Cr^{3+} area ratio was evaluated for different angles and over potentials, shown in Fig. 7b. For comparison, the ratio Cr^{6+}/Cr^{3+} expected for 0.3 nm $SrCrO_4$ on LSCr-Ni was plotted as well. With an over potential of -0.33 and -0.53 V vs O_2 the Cr^{6+} intensity relates reasonably well to the $SrCrO_4$ surface termination model, whereas for more reducing conditions with -1.03 and -1.48 V vs O_2 the Cr^{6+} component disappears mostly. In terms of chemical composition the $SrCrO_4$ is hard to proof or disproof because Sr is very often strongly enriched also on phase pure perovskite surfaces.

4.3. Binding energies

In addition to the peak shape and position changes attributed to valence changes, also the peak positions of fixed valent elements (e.g. Sr) may change which cell voltage, although the working electrode is grounded, and voltage was applied to the reference electrode in order to avoid electrostatic energy shifts. As elaborated earlier, the applied voltage changes the oxygen partial pressure and thereby its chemical potential according to

$$\mu_O^{WE} = \mu_{ion} - 2\mu_e = \mu_O^{RE} + 2FU, \quad (2)$$

where μ_O^{RE} is the oxygen chemical potential of the pre-reduction conditions (-1.03 V vs O_2) and μ_{ion} and μ_e are the chemical potentials of oxygen anions and electronic charge carriers, respectively. The binding energy measured in a calibrated XPS analyser is always the energy difference between the emitted photoelectron and the Work function W

$$E_b = E_{core} - W. \quad (3)$$

Where E_b is the measured binding energy, and E_{core} the actual core level energy of an emitted photoelectron. Consequently, electrons emitted from the Fermi level always have exactly 0 eV binding energy. In many nonstoichiometric oxides, the Fermi level lies within the band gap and is connected to the electron chemical potential via

$$E_F - E_{vac} = W = \frac{\mu_e}{N_A}, \quad (4)$$

where E_{vac} is the energy of a resting electron above the electrode surface. The Fermi level is defined to be zero, due to the grounded working electrode, but its position relative to the vacuum level or valence band edge may change with voltage. Differentiation of Eq. (4) by U reveals

$$\frac{d(E_F - E_{vac})}{dU} = \frac{dW}{dU} = -\frac{1}{N_A} \frac{d\mu_e}{dU}. \quad (5)$$

By differentiating Eq. (2) we get

$$\frac{1}{2} \frac{d\mu_{ion}}{dU} - \frac{d\mu_e}{dU} = F, \quad (6)$$

which can be transformed to

$$\frac{d\mu_e}{dU} = -F * \frac{\frac{d\mu_e}{dU}}{\frac{d\mu_e}{dU} - \frac{1}{2} \frac{d\mu_{ion}}{dU}}. \quad (7)$$

This expression combined with Eq. (5) yields

$$\frac{dW}{dU} = -\frac{F}{N_A} * \frac{\frac{d\mu_e}{dU}}{\frac{d\mu_e}{dU} - \frac{1}{2} \frac{d\mu_{ion}}{dU}}. \quad (8)$$

In Eq. (8), the terms $d\mu_e/dU$ and $d\mu_{ion}/dU$ have opposite signs. Consequently dW/dU and therefore the change of measured binding energy with voltage is equal or less than $-F/N_A$, or -1 eV/V.

The exact magnitude of the binding energy shift depends on the material's defect chemistry, which shall be exemplified with a simple defect chemical model. This model assumes that there are only two relevant point defect species, namely electronic point defects and oxygen vacancies of normalized concentration c . In such a model the chemical potentials of electrons and oxygen anions can be calculated as $\mu_e = \mu_e^0 + RT \ln(c_e)$ and $\mu_{ion} = \mu_{ion}^0 - RT \ln(c_{V_O})$. When such an electrode is polarized, the chemical potentials of electrons and oxygen anions change according to:

$$\begin{aligned} \frac{d\mu_e}{dU} &= \frac{RT}{c_e} \frac{dc_e}{dc_O} \frac{dc_O}{dU} \\ \frac{d\mu_{ion}}{dU} &= -\frac{RT}{c_{V_O}} \frac{dc_{V_O}}{dc_O} \frac{dc_O}{dU} \end{aligned} \quad (9)$$

Using the relations $dc_{V_O} = -dc_O$ and the differential form of the charge neutrality condition $dc_e = -2dc_O$ we can insert these terms into Eq. (8) to get

$$\frac{1}{N_A} \frac{d\mu_{eon}}{dU} = -\frac{dW}{dU} = \frac{dE_b}{dU} = -e \frac{\frac{1}{c_{eon}}}{\frac{1}{c_{eon}} + \frac{1}{4c_{V_O}}} \quad (10)$$

simplified to:

$$\begin{aligned} c_{eon} \gg 4c_{V_O}: \quad \frac{dE_b}{dU} &\approx 0 \frac{eV}{V} \\ c_{eon} \ll 4c_{V_O}: \quad \frac{dE_b}{dU} &\approx -1 \frac{eV}{V} \end{aligned} \quad (11)$$

Therefore, in oxides with mainly ionic defects, such as LSF64 or STF73 at low oxygen partial pressures, the Work function and XPS binding energy depend strongly on the applied voltage. In oxides with mainly electronic defects, and few oxygen vacancies such as manganite or chromates perovskites at higher oxygen partial pressures, the Work function should be almost independent of the applied voltage.

In Fig. 8 the binding energies of the Ti2p and Sr3d peaks for STF73 LSF64 are plotted as a function of applied voltage and slopes very close to -1 eV/V were measured, although the working electrode remained on ground potential. Therefore, the oxygen chemical potential changes by cell voltage affect primarily the electron chemical potential. This shows that the concentration of oxygen vacancies at the surface is much larger than the electron concentration in the investigated pO_2 range. For the bulk, this defect chemical regime is also predicted from electrochemical and thermogravimetric literature data [24,27,28]. Shifting binding energies were also already found in ambient pressure XPS for these materials [12]. Moreover, we can confirm that applying voltage to

the cell changes the reference electrode μ_O only negligibly. Also, we did not observe any drift in the binding energies with time, which confirms that for the duration of the experiment oxygen exchange reactions with the remaining gas phase were slow enough to not cause a measurable drift of the oxygen chemical potential in our cell. The binding energy vs over potential relation does not so nicely fit the simple defect chemical model for LSCr-Ni, see Fig. 8c. All observed elements shift with equal slopes of approx. -0.5 eV/V, which are slightly steeper in more reducing conditions. In Sr-doped lanthanum chromites the oxygen vacancy formation enthalpy is much larger and hence the transition between electronic and ionic compensation of the dopant charge occurs at a significantly more reducing oxygen pressure or over potential [39,40]. At higher oxygen partial pressures in the defect regime of mainly electronic charge compensation with a small amount of oxygen vacancies, the chemical potential of electrons should only change marginally upon application of a bias. In very reducing conditions, the dopant charge is mainly compensated by oxygen vacancies, with a small amount of electronic defects. Then the slope should switch to -1 eV/V, with a rather sharp bending. In contrast to this model we observe only weakly bias dependent slopes of about -0.5 eV/V, which are not in line with the defect model. However, the defect chemical considerations assumed non-interacting point defects and neglected surface effects, such as differing surface and bulk redox enthalpies and the probable formation of a $SrCrO_4$ termination. Hence, a simple point defect model is most likely insufficient to describe the actual defect chemistry of the LSCr-Ni surface.

5. Conclusion

Mixed conducting perovskite-type oxides are materials candidates for SOFC anodes, or SOEC cathodes. In a regular UHV chamber equipped with sample heating and electrical contacts, electrochemical XPS measurements were carried out on such materials. An optimised electrochemical model cell with thin film working electrode was used. Thanks to the comparatively large oxygen buffering capacity of the thick film counter electrode, it could be simultaneously used as the reference electrode with constant oxygen chemical potential. The initial oxygen nonstoichiometry was established in a pre-reduction step, in order to avoid O_2 release in UHV at high temperature. By heating the cell and applying voltage in UHV, the oxygen partial pressure in the investigated thin film working electrode bulk could be controlled within the range that is typical for SOFC anodes or SOEC cathodes. This measurement method proved to be very well suited for studying transition metal oxidation states and exsolution of Fe^0 and Ni^0 phases, and results fit excellently to those gained by synchrotron-based ambient

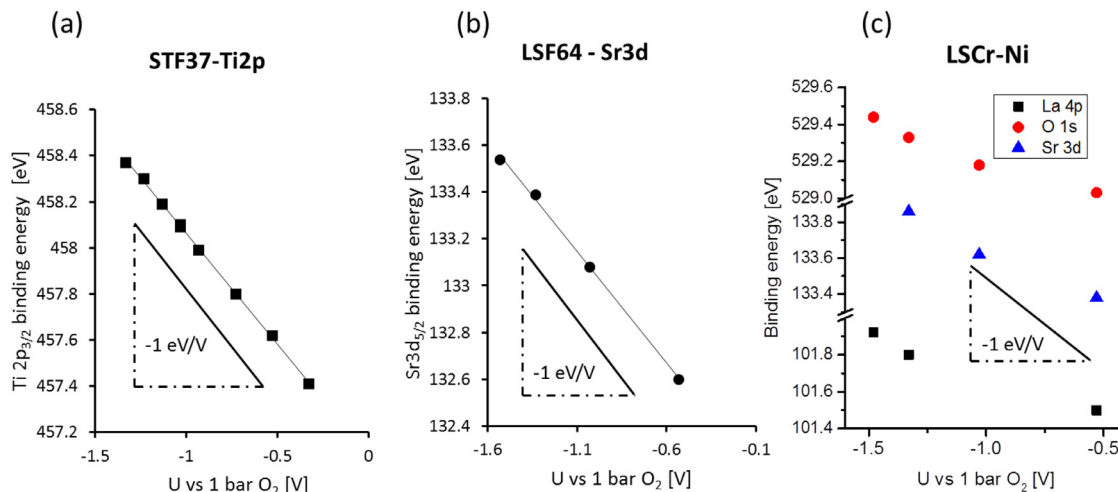


Fig. 8. The measured dependence of measured binding energy vs over potential on STF37 (a), LSF64 (b) and $La_{0.7}Sr_{0.2}Cr_{0.9}Ni_{0.1}O_{3.8}$ (c).

pressure XPS. However, information on surface catalytic properties, atmospheric adsorbates and reaction intermediates can only be gained with a surrounding atmosphere in ambient pressure XPS. Specifically, we found that for the electrode materials $\text{SrTi}_{0.3}\text{Fe}_{0.7}\text{O}_{3-\delta}$ and $\text{La}_{0.6}\text{Sr}_{0.4}\text{FeO}_{3-\delta}$ the oxidation states of near surface Fe depend on the cell voltage. Depending on the electrochemical polarisation, Fe^{3+} , Fe^{2+} and Fe^0 (the last in form of metallic particles) can be found on the electrode surface. The results were in good agreement with a previous near-ambient pressure XPS study of these materials in $\text{H}_2 + \text{H}_2\text{O}$ atmosphere, despite the fundamentally different atmospheric environments of ambient pressure XPS and UHV XPS. This indicates that the oxidation states of near-surface iron are primarily determined by the oxygen partial pressure in the electrode bulk than to the surrounding atmosphere.

On A-site deficient $\text{La}_{0.7}\text{Sr}_{0.2}\text{Cr}_{0.9}\text{Ni}_{0.1}\text{O}_{3-\delta}$ (LSCr-Ni) a Cr^{6+} species is present at over potentials much smaller than -1 V vs O_2 . In accordance with literature data on the phase stability of $(\text{La,Sr})\text{CrO}_3$, this species is most likely caused by a of SrCrO_4 surface termination. Hence, in contrast to STF, LSF and other oxides, A-site sub-stoichiometric LSCr-Ni exhibits a surface which is more oxidized than the bulk. Similar to the behaviour of Fe in LSF and STF, Ni particles evolve at the sample surface of LSCr-Ni during reduction in $\text{H}_2 + \text{H}_2\text{O}$ atmosphere. These particles can be reversibly oxidized and reduced by polarization of the cell in UHV.

The oxygen chemical potential in the working electrode changes with the cell voltage, which causes a change of the work function and results in a detectable shift of measured binding energies in the electrically grounded working electrode. As expected from defect chemical models of STF and LSF we observed a binding energy shift of -1 eV/V for electrically grounded STF and LSF working electrodes. On LSCr-Ni, the surface chemistry is more complex, due to the suggested formation of a SrCrO_4 termination, and a binding energy slope of roughly -0.5 eV/V was found. All together, these exemplary studies reveal that the oxygen partial pressure in solid oxide electrodes can be precisely controlled also in an UHV-based XPS setup when a heated solid oxide cell with a properly oxygen buffering reference electrode is used.

Acknowledgements

We thank the Austrian Science Fund (FWF) through grants F4509-N16 (SFB FOXSI) and W1243 (Solids4Fun) for financial support of this study. We also thank Johannes Frank, Wolfgang Werner, Annette Foelske-Schmitz, Markus Sauer and Roland Leber for their enduring work in setting up the XPS analyser at the “Analytical Instrumentation Center at TU Vienna”.

Supplementary materials

Supplementary material associated with this article can be found, in the online version, at [doi:10.1016/j.susc.2018.10.006](https://doi.org/10.1016/j.susc.2018.10.006).

References

- W.C. Chueh, Y. Hao, W. Jung, S.M. Haile, High electrochemical activity of the oxide phase in model ceria–Pt and ceria–Ni composite anodes, *Nat. Mater.* 11 (2012) 155–161.
- Y. Chen, W. Jung, Z. Cai, J.J. Kim, H.L. Tuller, B. Yildiz, Impact of Sr segregation on the electronic structure and oxygen reduction activity of $\text{SrTi}_{1-x}\text{Fe}_x\text{O}_3$ surfaces, *Energy Environ. Sci.* 5 (2012) 7979–7988.
- N. Tsvetkov, Q. Lu, B. Yildiz, Improved electrochemical stability at the surface of $\text{La}_{0.8}\text{Sr}_{0.2}\text{CoO}_3$ achieved by surface chemical modification, *Faraday Discuss.* 182 (2015) 257–269.
- E.J. Crumlin, H. Bluhm, Z. Liu, In situ investigation of electrochemical devices using ambient pressure photoelectron spectroscopy, *J. Electron Spectrosc. Related Phenom.* 190 (2013) 84–92.
- D. Starr, Z. Liu, M. Hävecker, A. Knop-Gericke, H. Bluhm, Investigation of solid/vapor interfaces using ambient pressure X-ray photoelectron spectroscopy, *Chem. Soc. Rev.* 42 (2013) 5833–5857.
- Z.A. Feng, M.L. Machala, W.C. Chueh, Surface electrochemistry of CO_2 reduction and CO oxidation on Sm-doped CeO_{2-x} : coupling between Ce^{3+} and carbonate adsorbates, *Phys. Chem. Chem. Phys.* 17 (2015) 12273–12281.
- W.C. Chueh, A.H. McDaniel, M.E. Grass, Y. Hao, N. Jabeen, Z. Liu, S.M. Haile, K.F. McCarty, H. Bluhm, F. El Gabaly, Highly enhanced concentration and stability of reactive Ce^{3+} on doped CeO_2 surface revealed in operando, *Chem. Mater.* 24 (2012) 1876–1882.
- Z.A. Feng, F. El Gabaly, X. Ye, Z.-X. Shen, W.C. Chueh, Fast vacancy-mediated oxygen ion incorporation across the ceria–gas electrochemical interface, *Nature Commun.* 5 (2014) 4374.
- Y. Yu, B. Mao, A. Geller, R. Chang, K. Gaskell, Z. Liu, B.W. Eichhorn, CO_2 activation and carbonate intermediates: an operando AP-XPS study of CO_2 electrolysis reactions on solid oxide electrochemical cells, *Phys. Chem. Chem. Phys.* 16 (2014) 11633–11639.
- C. Zhang, M.E. Grass, Y. Yu, K.J. Gaskell, S.C. DeCaluwe, R. Chang, G.S. Jackson, Z. Hussain, H. Bluhm, B.W. Eichhorn, Multielement activity mapping and potential mapping in solid oxide electrochemical cells through the use of operando XPS, *ACS Catalysis* 2 (2012) 2297–2304.
- S.C. DeCaluwe, M.E. Grass, C. Zhang, F.E. Gabaly, H. Bluhm, Z. Liu, G.S. Jackson, A.H. McDaniel, K.F. McCarty, R.L. Farrow, In situ characterization of ceria oxidation states in high-temperature electrochemical cells with ambient pressure XPS, *J. Phys. Chem. C* 114 (2010) 19853–19861.
- A. Nennung, A. Opitz, C. Rameshan, R. Rameshan, R. Blume, M. Hävecker, A. Knop-Gericke, G. Rupprechter, B. Klötzer, J. Fleig, Ambient pressure XPS study of mixed conducting perovskite-type SOFC cathode and anode materials under well-defined electrochemical polarization, *J. Phys. Chem. C* 120 (2016) 1461–1671.
- E.J. Crumlin, E. Mutoro, W.T. Hong, M.D. Biegalski, H.M. Christen, Z. Liu, H. Bluhm, Y. Shao-Horn, In situ ambient pressure x-ray photoelectron spectroscopy of cobalt perovskite surfaces under cathodic polarization at high temperatures, *J. Phys. Chem. C* 117 (2013) 16087–16094.
- D.N. Mueller, M.L. Machala, H. Bluhm, W.C. Chueh, Redox activity of surface oxygen anions in oxygen-deficient perovskite oxides during electrochemical reactions, *Nat. Commun.* 6 (2015) 6097.
- A.K. Opitz, A. Nennung, C. Rameshan, R. Rameshan, R. Blume, M. Hävecker, A. Knop-Gericke, G. Rupprechter, J. Fleig, B. Klötzer, Enhancing electrochemical water-splitting kinetics by polarization-driven formation of near-surface iron (0): an in situ xps study on perovskite-type electrodes, *Angew. Chemie Int. Ed.* 54 (2015) 2628–2632.
- A.K. Opitz, A. Nennung, C. Rameshan, M. Kubicek, T. Götsch, R. Blume, M. Hävecker, A. Knop-Gericke, G.N. Rupprechter, B. Klötzer, Surface chemistry of perovskite-type electrodes during high temperature CO_2 electrolysis investigated by operando photoelectron spectroscopy, *ACS Appl. Mater. Interfaces* 9 (2017) 35847–35860.
- M. Kubicek, G.M. Rupp, S. Huber, A. Penn, A.K. Opitz, J. Bernardi, M. Stöger-Pollach, H. Hutter, J. Fleig, Cation diffusion in $\text{La}_{0.6}\text{Sr}_{0.4}\text{CoO}_{3-\delta}$ below 800°C and its relevance for Sr segregation, *Phys. Chem. Chem. Phys.* 16 (2014) 2715–2726.
- M. Kubicek, A. Limbeck, T. Frömling, H. Hutter, J. Fleig, Relationship between cation segregation and the electrochemical oxygen reduction kinetics of $\text{La}_{0.6}\text{Sr}_{0.4}\text{CoO}_{3-\delta}$ thin film electrodes, *J. Electrochem. Soc.* 158 (2011) B727–B734.
- S. Adler, Reference electrode placement in thin solid electrolytes, *J. Electrochem. Soc.* 149 (2002) E166–E172.
- W.C. Jung, H.L. Tuller, Investigation of cathode behavior of model thin-film $\text{SrTi}_{1-x}\text{Fe}_x\text{O}_{3-\delta}$ ($x = 0.35$ and 0.5) mixed ionic-electronic conducting electrodes, *J. Electrochem. Soc.* 155 (2008) B1194–B1201.
- J. Fleig, F.S. Baumann, V. Brichzin, H.R. Kim, J. Jamnik, G. Cristiani, H.U. Habermeier, J. Maier, Thin film microelectrodes in SOFC electrode research, *Fuel Cells* 6 (2006) 284–292.
- F. Baumann, J. Maier, J. Fleig, The polarization resistance of mixed conducting SOFC cathodes: a comparative study using thin film model electrodes, *Solid State Ionics* 179 (2008) 1198–1204.
- W.C. Chueh, S.M. Haile, Electrochemical studies of capacitance in cerium oxide thin films and its relationship to anionic and electronic defect densities, *Phys. Chem. Chem. Phys.* 11 (2009) 8144–8148.
- A. Nennung, L. Volgger, E. Miller, L.V. Moggi, S. Barnett, J. Fleig, The electrochemical properties of Sr (Ti, Fe) $\text{O}_{3-\delta}$ for anodes in solid oxide fuel cells, *J. Electrochem. Soc.* 164 (2017) F364–F371.
- J. Jamnik, J. Maier, Generalised equivalent circuits for mass and charge transport: chemical capacitance and its implications, *Phys. Chem. Chem. Phys.* 3 (2001) 1668–1678.
- W. Lai, S.M. Haile, Impedance spectroscopy as a tool for chemical and electrochemical analysis of mixed conductors: a case study of ceria, *J. Am. Ceram. Soc.* 88 (2005) 2979–2997.
- M. Kuhn, S. Hashimoto, K. Sato, K. Yashiro, J. Mizusaki, Oxygen nonstoichiometry, thermo-chemical stability and lattice expansion of $\text{La}_{0.6}\text{Sr}_{0.4}\text{FeO}_{3-\delta}$, *Solid State Ionics* 195 (2011) 7–15.
- M. Kuhn, J.J. Kim, S.R. Bishop, H.L. Tuller, Oxygen nonstoichiometry and defect chemistry of perovskite-structured $\text{Ba}_{0.9}\text{Sr}_{1-x}\text{Ti}_{1-y}\text{Fe}_y\text{O}_{3-y/2+\delta}$ solid solutions, *Chem. Mater.* 25 (2013) 2970–2975.
- M. Descostes, F. Mercier, N. Thomat, C. Beaucaire, M. Gautier-Soyer, Use of XPS in the determination of chemical environment and oxidation state of iron and sulfur samples: constitution of a data basis in binding energies for Fe and S reference compounds and applications to the evidence of surface species of an oxidized pyrite in a carbonate medium, *Appl. Surface Sci.* 165 (2000) 288–302.
- C. Arrivé, T. Delahaye, O. Joubert, G. Gauthier, Exsolution of nickel nanoparticles at the surface of a conducting titanate as potential hydrogen electrode material for solid oxide electrochemical cells, *J. Power Sour.* 223 (2013) 341–348.
- D. Neagu, G. Tsekouras, D.N. Miller, H. Ménard, J.T.S. Irvine, In situ growth of

- nanoparticles through control of non-stoichiometry, *Nat Chem* 5 (2013) 916–923.
- [32] D. Neagu, T.-S. Oh, D.N. Miller, H. Ménard, S.M. Bukhari, S.R. Gamble, R.J. Gorte, J.M. Vohs, J.T. Irvine, Nano-socketed nickel particles with enhanced coking resistance grown in situ by redox exsolution, *Nat. Commun.* 6 (2015) 8120.
- [33] D. Neagu, T.-S. Oh, D.N. Miller, H. Ménard, S.M. Bukhari, S.R. Gamble, R.J. Gorte, J.M. Vohs, J.T. Irvine, Nano-socketed nickel particles with enhanced coking resistance grown in situ by redox exsolution, *Nat. Commun.* 6 (2015) 8120.
- [34] N. McIntyre, M. Cook, X-ray photoelectron studies on some oxides and hydroxides of cobalt, nickel, and copper, *Anal. Chem.* 47 (1975) 2208–2213.
- [35] G. Allen, P. Tucker, Multiplet splitting of X-ray photoelectron lines of chromium complexes. The effect of covalency on the 2p core level spin-orbit separation, *Inorg. Chim. Acta* 16 (1976) 41–45.
- [36] W.-Y. Hwang, R. Thorn, Investigation of the electronic structure of $\text{La}_{1-x}(\text{M}^{2+})_x\text{CrO}_3$, Cr_2O_3 and La_2O_3 by X-ray photoelectron spectroscopy, *J. Phys. Chem. Solids* 41 (1980) 75–81.
- [37] S. Tanuma, C.J. Powell, D.R. Penn, Calculation of electron inelastic mean free paths (IMFPs) VII. Reliability of the TPP-2M IMFP predictive equation, *Surf. Interface Anal.* 35 (2003) 268–275.
- [38] S. Miyoshi, S. Onuma, A. Kaimai, H. Matsumoto, K. Yashiro, T. Kawada, J. Mizusaki, H. Yokokawa, Chemical stability of $\text{La}_{1-x}\text{Sr}_x\text{CrO}_3$ in oxidizing atmospheres, *J. Solid State Chem* 177 (2004) 4112–4118.
- [39] J.W. Fergus, Lanthanum chromite-based materials for solid oxide fuel cell interconnects, *Solid State Ionics* 171 (2004) 1–15.
- [40] S. Onuma, K. Yashiro, S. Miyoshi, A. Kaimai, H. Matsumoto, Y. Nigara, T. Kawada, J. Mizusaki, K. Kawamura, N. Sakai, Oxygen nonstoichiometry of the perovskite-type oxide $\text{La}_{1-x}\text{Ca}_x\text{CrO}_{3-\delta}$ ($x = 0.1, 0.2, 0.3$), *Solid State Ionics* 174 (2004) 287–293.